



Fenretinide induces a new form of dynamin-dependent cell death in pediatric sarcoma

Eva Brack¹ · Marco Wachtel¹ · Anja Wolf¹ · Andres Kaech² · Urs Ziegler² · Beat W. Schäfer¹

Received: 26 June 2019 / Revised: 18 February 2020 / Accepted: 18 February 2020 / Published online: 6 March 2020
© The Author(s), under exclusive licence to ADMC Associazione Differenziamento e Morte Cellulare 2020

Abstract

Alveolar rhabdomyosarcoma (aRMS) is a highly malicious childhood malignancy characterized by specific chromosomal translocations mostly encoding the oncogenic transcription factor PAX3-FOXO1 and therefore also referred to as fusion-positive RMS (FP-RMS). Previously, we have identified fenretinide (retinoic acid p-hydroxyanilide) to affect PAX3-FOXO1 expression levels as well as FP-RMS cell viability. Here, we characterize the mode of action of fenretinide in more detail. First, we demonstrate that fenretinide-induced generation of reactive oxygen species (ROS) depends on complex II of the mitochondrial respiratory chain, since ROS scavenging as well as complexing of iron completely abolished cell death. Second, we co-treated cells with a range of pharmacological inhibitors of specific cell death pathways including z-vad (apoptosis), necrostatin-1 (necroptosis), 3-methyladenine (3-MA) (autophagy), and ferrostatin-1 (ferroptosis) together with fenretinide. Surprisingly, none of these inhibitors was able to prevent cell death. Also genetic depletion of key players in the apoptotic and necroptotic pathway (BAK, BAX, and RIPK1) confirmed the pharmacological data. Interestingly however, electron microscopy of fenretinide-treated cells revealed an excessive accumulation of cytoplasmic vacuoles, which were distinct from autophagosomes. Further flow cytometry and fluorescence microscopy experiments suggested a hyperstimulation of macropinocytosis, leading to an accumulation of enlarged early and late endosomes. Surprisingly, pharmacological inhibition as well as genetic depletion of large dynamin GTPases completely abolished fenretinide-induced vesicle formation and subsequent cell death, suggesting a new form of dynamin-dependent programmed cell death. Taken together, our data identify a new form of cell death mediated through the production of ROS by fenretinide treatment, highlighting the value of this compound for treatment of sarcoma patients including FP-RMS.

Introduction

Rhabdomyosarcoma (RMS) is the most common soft tissue malignancy of children and young adolescents accounting for 5–10% of all cancers in this age group [1]. RMS are highly malignant tumors of mesenchymal cell origin that

can be subdivided into two major subtypes, of which alveolar rhabdomyosarcoma (aRMS) is the most unfavorable one [2]. The majority of aRMS are characterized by a tumor-specific chromosomal translocation generating the chimeric transcription factor PAX3/7-FOXO1 (fusion-positive RMS or FP-RMS) [3]. The overall survival rate of patients suffering from this malignancy is poor with less than 30%, and the recurrence rate is high with more than 48%. Further, the remaining 5-year post relapse survival rate is only about 21% [2, 4]. Resistance of FP-RMS to conventional treatments including chemotherapy and radiation therapy, which mainly lead to induction of apoptosis, is a main cause of failure [5–7]. Hence, one of the major resistance mechanisms is the intrinsic or acquired ability to prevent apoptosis [8].

During the last decade a range of nonapoptotic cell death pathways have been described [9], opening the exciting possibility to eliminate cancer cells via alternative routes. Besides apoptosis, regulated necrosis, including necroptosis,

Edited by E. Baehrecke

Supplementary information The online version of this article (<https://doi.org/10.1038/s41418-020-0518-z>) contains supplementary material, which is available to authorized users.

✉ Beat W. Schäfer
beat.schaefer@kispi.uzh.ch

¹ Department of Oncology and Children's Research Center, University Children's Hospital Zurich, Zurich, Switzerland

² Center for Microscopy and Image Analysis, University of Zurich, Zurich, Switzerland

and ferroptosis, are the most studied alternative forms of cell death [10]. A number of compounds are available that can activate such alternative death pathways [11–16] and thereby have an antineoplastic action.

Several types of cell death are associated with accumulation of cytoplasmic vesicles including methuosis, paraptosis, or oncosis [17–24]. Methuosis is a recently described form of cell death and is characterized by an accumulation of phase lucent vesicles generated by increased macrophagocytosis. This type of cell death is now investigated in different cancers where it can be induced through multiple compounds such as vacuolin-1 [17–20]. However, a cell death mode characterized by accumulation of vacuoles has not yet been reported for FP-RMS.

To explore cell death inducing agents specifically in FP-RMS, we previously screened a library of 1280 mostly Food and Drug Administration (FDA)-approved compounds using PAX3-FOXO1 activity as read-out [25]. From this screen, we identified fenretinide (retinoic acid p-hydroxyanilide) as one of the most effective small-molecule compounds inducing a strong reduction of FP-RMS tumor growth in mouse xenograft experiments.

Here, we therefore investigated the detailed mechanism of cell death provoked by fenretinide in FP-RMS cells. The compound activated a novel form of nonapoptotic cell death associated with extensive accumulation of cytoplasmic vesicles [17, 26]. Strikingly, this depended pharmacologically and genetically on the function of dynamin GTPases, known regulators of endocytosis. These findings, together with a long experience of fenretinide treatment in clinics for the treatment of multiple malignancies, rejuvenate the application of this compound in FP-RMS.

Results

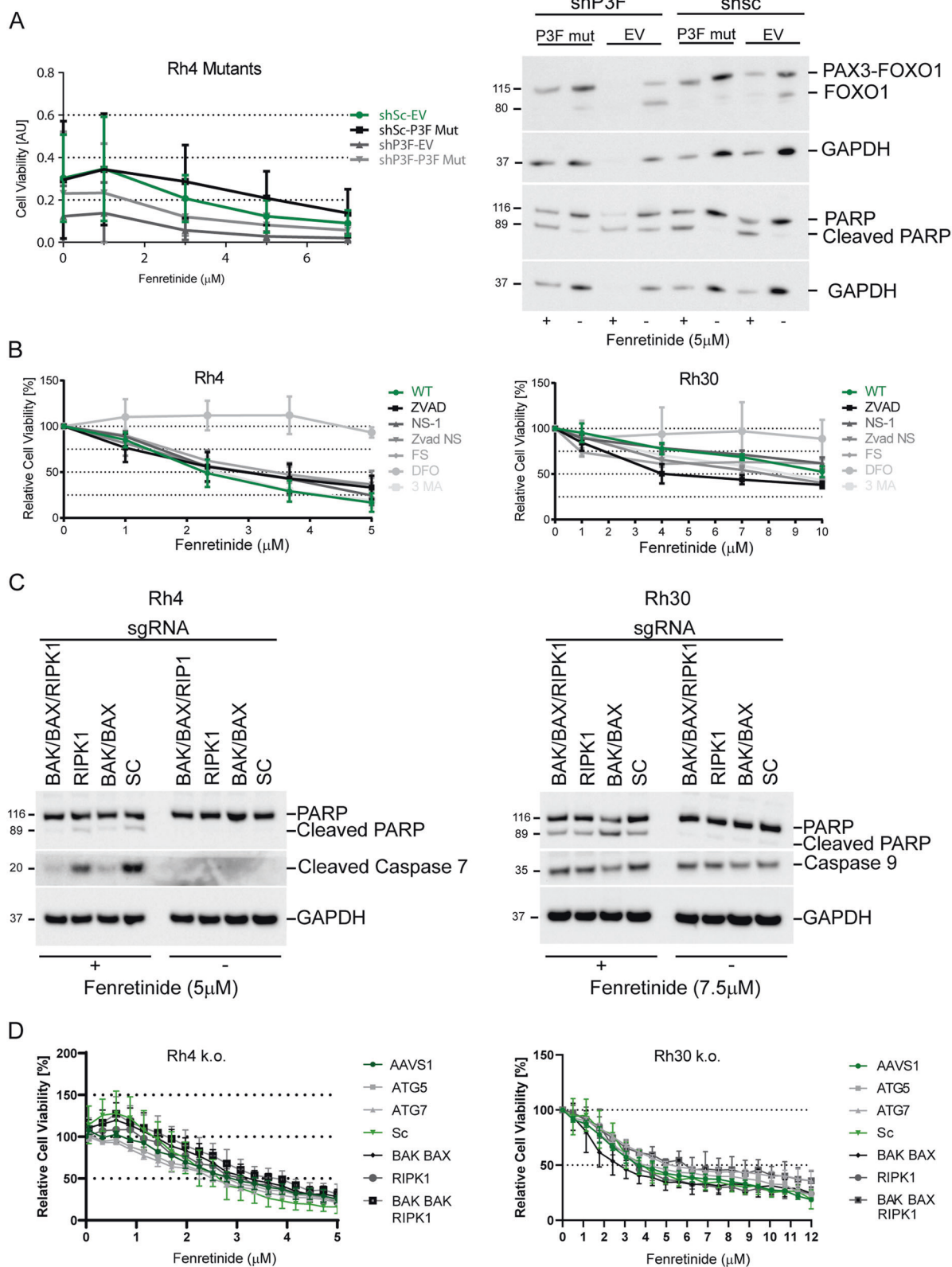
Fenretinide activates a nonclassical cell death pathway

We previously demonstrated that fenretinide-induced cell death was associated with a reduction in PAX3-FOXO1 levels [25]. Since expression of PAX3-FOXO1 is required for survival [27], we first explored whether the effect of fenretinide is dependent on fusion protein depletion. For this, we used a doxycycline inducible lentiviral shRNA vector directed against endogenous PAX3-FOXO1 (Supplementary Fig. 1A) together with a EF1-promoter driven vector for expression of an shRNA-insensitive variant of PAX3-FOXO1 (P3F mut) in Rh4 cells [28]. Upon induction of shRNA, endogenous P3F protein levels were reduced to about 20%, while levels of ectopic PAX3-FOXO1 matched the ones of the endogenous protein. Physiologically, ectopic expression of PAX3-FOXO1 reduced the levels of cleaved

PARP, suggesting that this can rescue cells from apoptosis. Unexpectedly however, ectopic PAX3-FOXO1 did not protect from fenretinide-induced cell death as measured by the water-soluble tetrazolium-1 (WST-1) assay and western blotting (Fig. 1a and Supplementary Fig. 1B), despite maintaining exogenous PAX3-FOXO1 protein levels. These results suggest that induction of apoptosis after fenretinide treatment is linked to a reduction in PAX3-FOXO1 levels, while under conditions of sustained PAX3-FOXO1 expression fenretinide induces an alternative mode of cell death.

To explore this hypothesis further, we next studied different well-characterized cell death pathways to evaluate their relevance for fenretinide-mediated cytotoxicity using a pharmacological approach. We treated two FP-RMS cell lines (Rh4 and Rh30) with fenretinide in combination with the apoptosis inhibitor z-vad, the necroptosis inhibitor necrostatin (NS-1), the autophagy inhibitor 3-methyladenine (3-MA), the ferroptosis inhibitor ferrostatin-1 (FS), and the iron chelator deferoxamine (DFO) [29, 30] and assessed cell viability after 48 h. Surprisingly, none of the specific cell death inhibitors was able to rescue from cell death (Fig. 1b), suggesting that neither induction of apoptosis, necroptosis, ferroptosis, or autophagy play a major role in fenretinide-induced cell death. Interestingly however, DFO almost completely rescued cell viability. While both FS and DFO act as reactive oxygen species (ROS) scavengers, FS is lipid-soluble and claimed to protect from membrane lipid-peroxidation during ferroptosis, while DFO has a more broad ROS-protecting activity, suggesting that more broadly produced ROS species might play an important role.

Since pharmacological inhibition is prone to certain off-target effects, we aimed next to confirm these results using a genetic approach. We used the CRISPR/Cas9 system in both cell lines to knock out the essential apoptotic/necroptotic/autophagic pathway genes to create death pathway ablated tumor cells. To block apoptosis, we combined sgRNAs directed against BAK and BAX, two key players in the intrinsic apoptotic pathway, to inhibit necroptosis we used sgRNAs directed against RIPK1, the central kinase in the necroptotic pathway and to block autophagy we knocked out ATG5 and 7. We achieved nearly complete knockouts for BAK and BAX as well as a significant reduction of RIPK1 and ATG5 and 7 as determined by western blot (Supplementary Fig. 1C). In parallel, we also depleted the three genes BAK, BAX, and RIPK1 in one single cell population. In Rh4 cells, combined knockout of BAX and BAK resulted in a nearly complete inhibition of caspase 7 and PARP-1 cleavage after fenretinide treatment, while in Rh30 cells both PARP-1 and caspase-9 cleavage were less affected by the genetic manipulations, suggesting that other apoptotic pathways are (also) involved. Similar results were seen for the triple knockouts of BAK/BAX/RIPK1 (Fig. 1c). Interestingly, we found that Rh4 cells do



not express caspase-8, while Rh30 cells do (Supplementary Fig. 1D) which might explain the differences in apoptotic downstream effects between the two cell lines. Next, we

determined dose-response curves with all knockout cells after fenretinide treatment. In agreement with the pharmacological approach, we observed only a very small,

◀ **Fig. 1 Fenretinide activates a distinct and nonclassical cell death pathway.** **a** Left panel: cell viability of indicated engineered Rh4 cells treated with doxycycline and increasing concentrations of fenretinide as determined by the WST assay. Right panel: western blot using whole-cell lysates from indicated modified Rh4 cells after treatment or not with 5 μ M fenretinide for 48 h. **b** Cell viability assay of Rh4 (left panel) and Rh30 (right panel) cells treated with increasing concentrations of fenretinide in combination with different cell death inhibitors (z-vad (100 μ M), NS-1 (25 μ M), 3-MA (2.5 μ M), FS (4 μ M), and DFO (50 μ M)). **c** Western blot using whole-cell lysates from Rh4 and Rh30 cells carrying the indicated knockouts treated with increasing concentrations of fenretinide. PARP cleavage and caspase 7 or 9 activity was assessed. **d** Cell viability assay of indicated knockout cells treated with increasing concentrations of fenretinide as assessed by the WST assay in Rh4 (left panel) and Rh30 (right panel) cells.

nonsignificant rescue from cell death in deleted versus wild-type cells, which was slightly more pronounced in the triple knockout cells (Fig. 1d). Nevertheless, these results suggest that while fenretinide engages some apoptotic features including caspase activation, cells execute mainly an alternative death pathway if apoptosis is blocked. To confirm, we performed time-lapse microscopy of wild type, as well as BAK/BAX knockout cells under fenretinide treatment and stained these for active caspase 3/7 and propidium iodide (PI). After 26 h, we observed similar numbers of cells staining positive for activated caspase and for PI, suggesting equal execution of apoptosis and an alternative form of cell death. This was also true for BAX/BAK knockout cells (Supplementary Fig. 2).

Fenretinide triggers production of ROS

Based on the ability of the ROS inhibitor DFO to rescue FP-RMS cells from fenretinide-induced cell death, we wondered whether ROS might be responsible for induction of cell death.

First, we observed a strong perinuclear accumulation of ROS with the fluorogenic pan-ROS probe CellRox after 20 h of fenretinide treatment (Fig. 2a). To evaluate its kinetics, we captured time-lapse fluorescence microscopy images of fenretinide-treated and untreated Rh4 cells. This revealed positively stained cells already 20 h after fenretinide treatment, which started to detach and undergo cell death 6 h later, demonstrating that ROS production precedes initiation of cell death. In BAK/BAX/RIPK1 knockout cells, the onset of cell death was delayed for about 10 h (Supplementary Fig. 3A), validating that fenretinide is able to initiate apoptosis, but cells undergo a different mode of cell death if apoptosis is blocked.

To quantify induced ROS, we measured CellRox fluorescence 18 h after fenretinide treatment by flow cytometry. This revealed that ROS levels increased by about 2.5 fold. Staining of cells with a mitochondria-specific ROS probe (MitoSox) showed a similar increase of about threefold

(Fig. 2b), suggesting that at least a part of fenretinide-induced ROS species originate from mitochondria.

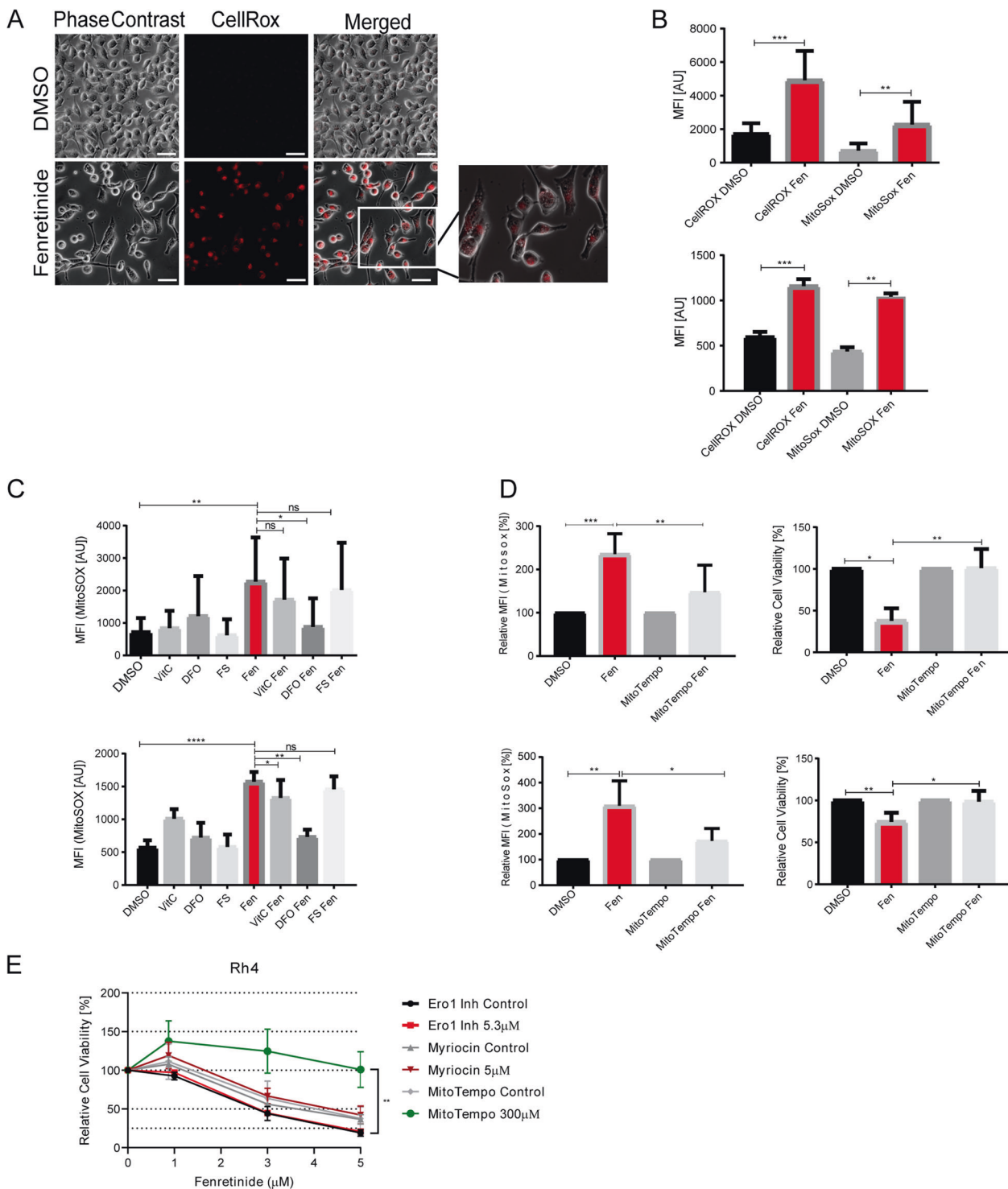
To determine the relevance of ROS for induction of cell death, we used different ROS inhibitors including the antioxidant vitamin C, DFO, FS, and the mitochondria-specific ROS scavenger MitoTempo. The extent of reduction in ROS levels differed, with DFO and MitoTempo reducing them below 50%, while vitamin C and FS were considerably less effective (Fig. 2c, d and Supplementary Fig. 3B). In agreement with these scavenging potencies, similar to DFO (Fig. 1b) also MitoTempo was able to completely inhibit fenretinide-induced cell death (Fig. 2d), while vitamin C and FS had only minor effects. These findings suggest that fenretinide induces mitochondrial ROS, which are involved in the induction of cell death. To evaluate the role of other sources of ROS such as lipid second messengers or the ER, we used inhibitors against the serine palmitoyltransferase (myriocin), and the endoplasmic reticulum oxidase (ERO1) in comparison with MitoTempo, co-treated our cells with fenretinide and assessed cell viability (Fig. 2e). Besides MitoTempo, none of these inhibitors rescued cells from fenretinide-mediated cell death suggesting that neither the sphingolipid pathway nor the endoplasmic reticulum are relevant sources of ROS. However, a complete rescue was achieved with MitoTempo, indicating that the mitochondria are sources of fenretinide-induced ROS.

Production of ROS depends on complex II of the mitochondrial respiratory chain (MRC)

One of the major sources of ROS production is the MRC. As the MRC is the major source of ATP production in the cell, any interference is fatal for the tumor cell and reduces the mitochondrial membrane potential ($\Delta\psi_m$). Hence, we next evaluated whether the mitochondrial ROS induced by fenretinide are produced by one of the MRC complexes. We co-treated Rh4 cells with fenretinide and different inhibitors targeting the five complexes of the MRC and measured the amount of produced ROS. Inhibitors against complex I (rotenone), III (antimycin), IV (sodium azide), and V (CCCP) did not cause a decrease in ROS levels (Supplementary Fig. 4). Instead, inhibitors of complex II, namely TTFA and carboxin significantly reduced ROS production in both Rh4 and Rh30 cells (Fig. 3a, b). These findings indicate that the main target of fenretinide for ROS production lies downstream of complex II of the MRC.

Fenretinide induces accumulation of cytoplasmic vesicles

To further characterize fenretinide-induced cell death, we next investigated morphological changes at the ultrastructural level



using electron microscopy (EM). For this, we treated Rh4 and Rh30 cells with fenretinide alone or in combination with z-vad for 48 h (Fig. 4a). Interestingly, this revealed that fenretinide induced an enormous vacuolization within the cytoplasm, which was even further enhanced in combination with z-vad. The vacuoles had different sizes, were phase lucent and contained only one single membrane, suggesting that they do

not represent autophagosomes. In contrast, features of apoptosis were only rarely detected, most pronounced in a combination of fenretinide with necrostatin (data not shown), whereas we could readily identify chromatin condensation and membrane blebbing after treatment with the PLK1 inhibitor volasertib, which is known to induce apoptosis in RMS cells [31] (Supplementary Fig. 5A). These findings further

Fig. 2 Fenretinide triggers the production of reactive oxygen species. **a–d** Fluorescence microscopy analysis and flow cytometry of fenretinide-treated Rh4 cells. **a** Light microscopy images of fenretinide (3 μ M) treated Rh4 cells stained with a fluorogenic Pan-ROS detectant (4 μ M CellRox). Scale bar is 50 μ m. **b** Mean fluorescence index analysis of the flow cytometry data of Rh4 (upper panel) and Rh30 cells (lower panel) treated with fenretinide (3 and 4 μ M, respectively). Cells were stained with 4 μ M CellRox and 10 μ M MitoSox for the detection of total ROS and mitochondrial ROS levels, respectively. **c** Mean fluorescence index analysis of the flow cytometry data of Rh4 (upper panel) and Rh30 (lower panel) cells treated with fenretinide (3 and 4 μ M, respectively) and different ROS inhibitors including vitamin C (50 μ M), deferoxamine (50 μ M), and ferostatin (4 μ M). Cells were stained with MitoSox for the detection of mitochondrial ROS levels. **d** Mean fluorescence index of the flow cytometry data of ROS levels in Rh4 and Rh30 cells (upper and lower panel, respectively) after indicated treatments (left panel) and cell viability of Rh4 and Rh30 cells treated with fenretinide (3 and 4 μ M, respectively) in the presence or absence of the mitochondria-specific ROS scavenger MitoTempo (300 μ M) as determined by WST assay (right panel). **e** Cell viability of Rh4 cells treated with increasing concentrations of fenretinide in combination with different compounds including an inhibitor of the sphingolipid pathway (myriocin (5 μ M)), an endoplasmic reticulum stress inhibitor (Ero1 (5.3 μ M)), and a ROS scavenger (MitoTempo (300 μ M)).

strengthen our hypothesis that fenretinide is able to trigger multiple types of cell death.

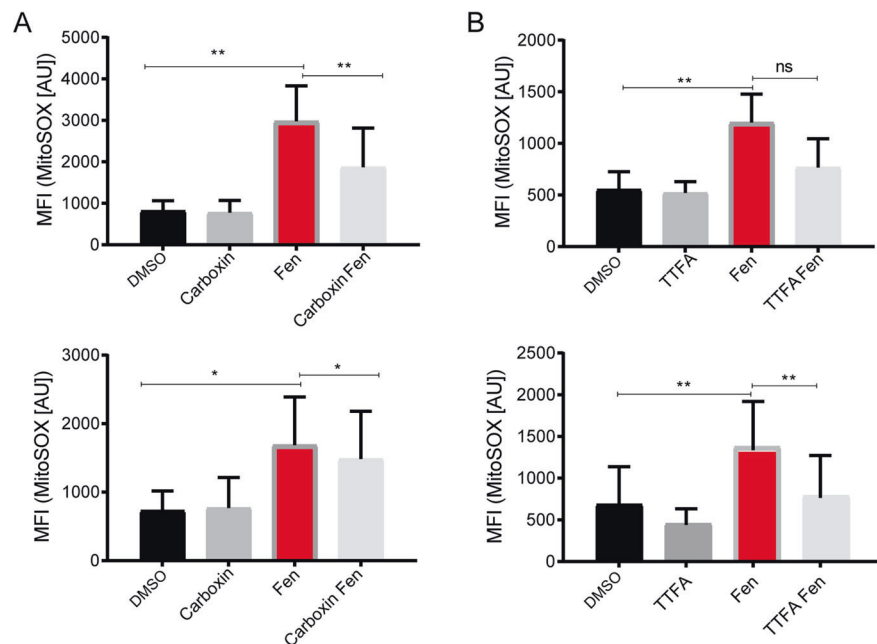
The observed features of the phase lucent vesicles were consistent with macropinosomes and reminiscent of cell death forms which are associated with accumulation of endosomes [17, 26]. We therefore wondered whether fenretinide-induced cell death involved disturbance of macropinocytosis or endocytosis. To study macropinocytosis, we followed the uptake of fluid phase dyes like acridine orange (AO) and lucifer yellow (LY) [20] by flow

cytometric analysis. Fenretinide indeed induced the uptake of AO and LY (>4-fold increase, Fig. 4b and Supplementary Fig. 5B, C). Co-treatment with the ROS scavengers vitamin C and MitoTempo almost completely abolished this uptake, indicating that the fenretinide-induced increase in dye uptake is downstream of ROS induction and mediated through macropinocytosis. Addition of z-vad to fenretinide-treated cells did not further enhance this effect. Validation of these results by fluorescent microscopy after 48 h fenretinide treatment confirmed the strong increase in LY uptake (Fig. 4c). Hence, these findings are in accordance with the EM images and suggest that the observed vesicles derive from an increased accumulation of endosomes, similar to the ones described for other cytoplasmic vacuolization associated cell death forms [17, 26, 32].

Fenretinide causes accumulation of early and late endosomes

To further characterize the endosomal origin of the vesicles, we stained fenretinide-treated cells with antibodies directed against the early endosomal marker Rab5, the late endosomal marker Rab7, and the lysosomal marker LAMP-1. Compared with untreated control, an accumulation of early and late endosomes but not of lysosomes was observed (Fig. 5a, upper and lower panel, and 5b). Interestingly, even though the vesicles are acidic enough to allow AO emission to change from green to red (Figs. 4b, 5e and Supplementary Fig. 5B, C), they are unable to further mature and fuse with lysosomes, indicating that later maturation steps are blocked.

Fig. 3 Fenretinide interferes with complex II of the mitochondrial respiratory chain. Flow cytometry analysis of fenretinide (3/4 μ M) treated Rh4 and Rh30 cells (upper and lower panel, respectively) in combination with two different inhibitors of complex II of the respiratory chain. Assessed was mitochondrial ROS by staining with MitoSox (10 μ M). **a** Mean fluorescence index of flow cytometry data measured in Rh4 and Rh30 cells treated with fenretinide in combination with 1500 μ M of complex II inhibitor carboxin and **b** 500 μ M or 1000 μ M TTFA.



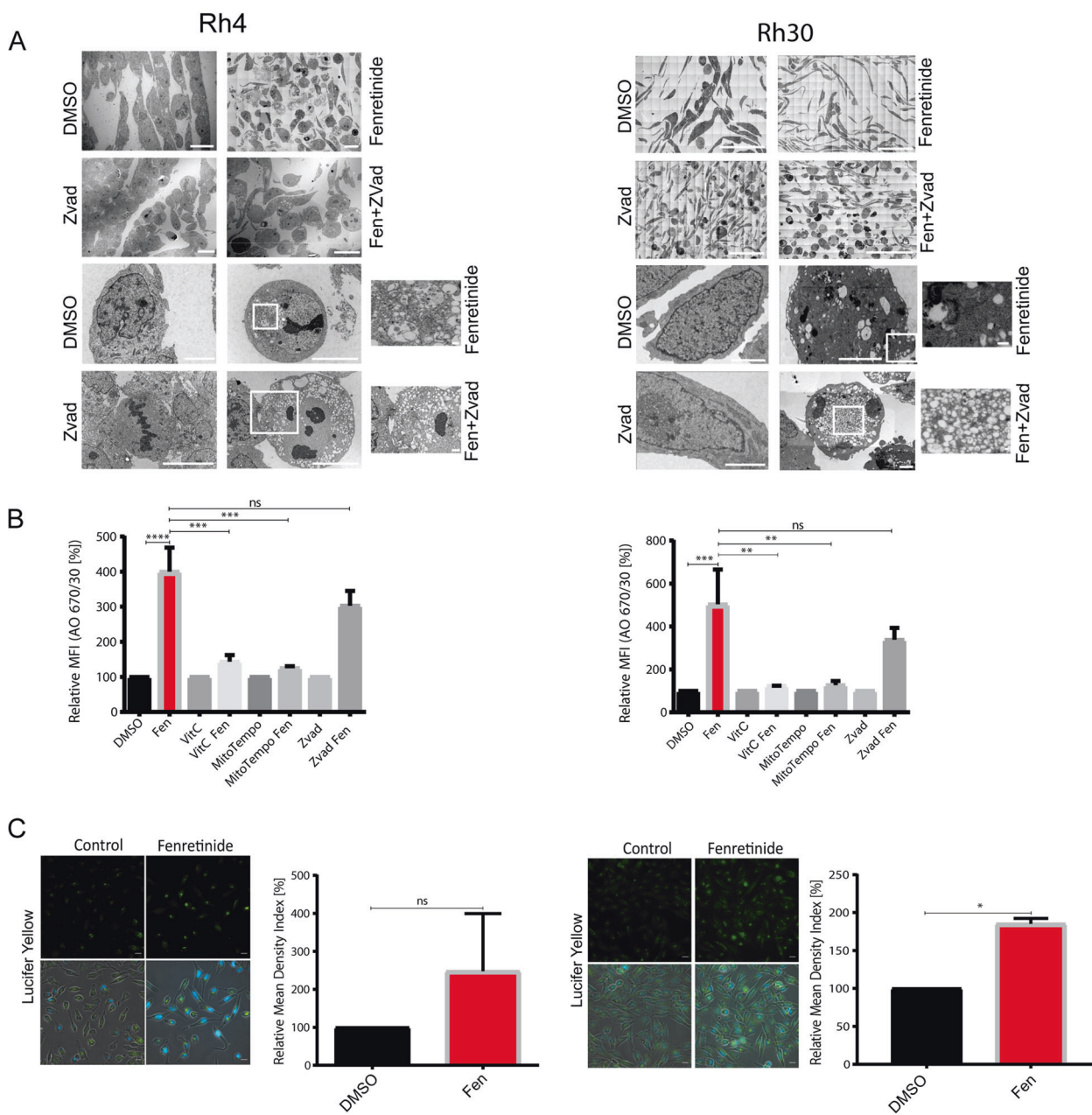
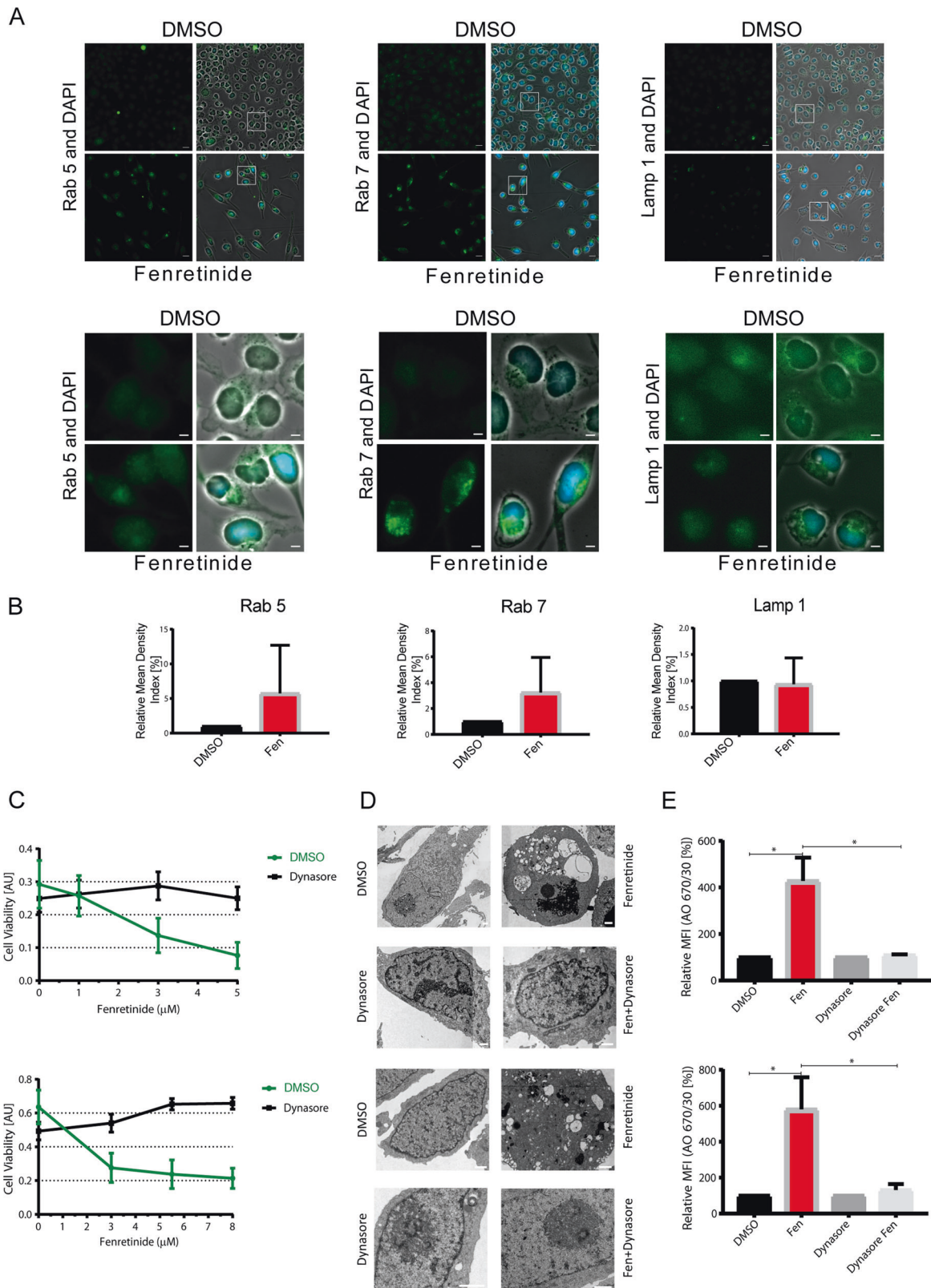


Fig. 4 Fenretinide induces accumulation of cytoplasmic vesicles and uptake of fluid phase dyes. **a** Electron microscopy images of untreated or fenretinide-treated Rh4 and Rh30 cells (3 and 4 μ M, respectively; left and right panel) for 48 h (first and third from top). Second and fourth from top are Rh4 and Rh30 cells treated with fenretinide (3 and 4 μ M, respectively) and z-vad (100 μ M) for 48 h. Scale bar is 2 μ m (Rh4) and 70 μ m (Rh30) for first and second, and 10 and 1 μ m (Rh4), and 30 and 3 μ m (Rh30) for third and fourth panel. **b** Mean fluorescence index of the flow cytometry data of fenretinide (3 and 4 μ M, respectively) treated Rh4 and Rh30 cells in combination with

different inhibitors including vitamin C (50 μ M), z-vad (100 μ M), and MitoTempo (300 μ M), stained with acridine orange (2.7 μ M) using two different bandpass filters 530/30 and 670/30 (See Supplementary Fig. 4B). **c** Fluorescence microscopy images of Rh4 and Rh30 cells left untreated or treated with fenretinide (3 and 4 μ M, respectively) and stained with lucifer yellow (820 μ M). Scale bar is 20 μ m. Graphs on the right show quantification of the relative mean density index assessed with Fiji software. Total integrated density value of an image was divided by the number of cells.

Based on this, we next aimed to further substantiate the relevance of disturbed endocytosis for fenretinide-induced cell death. We blocked the different endocytic processes by chemical compounds and measured cell viability. Neither inhibition of macropinocytosis by EIPA, clathrin-

independent endocytosis by filipin and genistein nor clathrin-mediated endocytosis by chlorpromazine influenced cell viability upon fenretinide treatment (Supplementary Fig. 6A). Interestingly however, the dynamin inhibitors dynasore and dyngo-4a nearly completely



rescued from cell death (Fig. 5c, d and Supplementary Fig. 6B), both at the physiological (Fig. 5c) and the morphological level (Fig. 5d). Moreover, we also

observed a significant inhibition of AO uptake by co-treatment with dynasore (Fig. 5e and Supplementary Fig. 6C).

◀ **Fig. 5 Fenretinide causes accumulation of early and late endosomes.** **a** Fluorescence images of Rh4 cells left untreated or treated with fenretinide (3 μ M) and stained with antibodies against either Rab5, Rab7, or Lamp-1. DAPI was used as nuclear stain. Scale bar is 20 μ m (upper panel) and 5 μ m for the magnified images (lower panel). **b** Quantification of the relative mean density index assessed with Fiji software. Total integrated density value of an image was divided by the number of cells. **c** Cell viability of Rh4 and Rh30 cells (upper and lower panel, respectively) treated with increasing concentrations of fenretinide in combination with 30 μ M of dynasore. **d** Electron microscopy images of untreated or fenretinide-treated Rh4 (3 μ M fenretinide) and Rh30 (4 μ M fenretinide) cells (upper and lower panel, respectively) for 48 h (lane one and three). Scale bar is 1 μ m. Lane two and four show Rh4 and Rh30 cells treated with fenretinide (3 and 4 μ M, respectively) and dynasore (30 μ M) for 48 h. **e** Relative mean fluorescence index of the flow cytometry data of fenretinide-treated Rh4 and Rh30 cells (upper, respective lower panel) in combination with the dynamin inhibitor dynasore (30 μ M), stained with acridine orange (2.7 μ M) using the two different bandpass filters 530/30 and 670/30 (see Supplementary Fig. 6C).

To exclude, that dynasore acts via ROS scavenging, we co-treated Rh4 and Rh30 cells and measured mitochondrial ROS after 48 h by flow cytometry. In Rh4 cells ROS levels were unaffected by dynasore, while we measured an almost 50% reduction in ROS levels in Rh30 cells (Supplementary Fig. 6D), suggesting that dynasore does not generally act as ROS scavenger and the reduction of ROS levels in Rh30 cells might occur indirectly.

To evaluate whether dynasore specifically rescued fenretinide-mediated cell death, we screened a small-molecule library with 204 mostly FDA-approved drugs in Rh4 cells alone and in combination with dynasore or vitamin C and assessed cell viability (Supplementary Fig. 6E). Within the top cytotoxic drugs (reducing viability to 15–55%), we identified ten drugs that exerted a ROS-dependent cytotoxic effect (cell viability change >25%), including MLN2238, MLN9708, rigosertib, verdinexor, BI-847325, ponatinib, MK-1775, VX-680, ispinesib, and elesclomol (Fig. 5e, right table). In none of these cases however, dynasore could significantly enhance survival, indicating that dynasore acts specifically on fenretinide-induced cell death and not simply as ROS scavenger.

Fenretinide-induced vesicle formation depends on dynamin GTPases

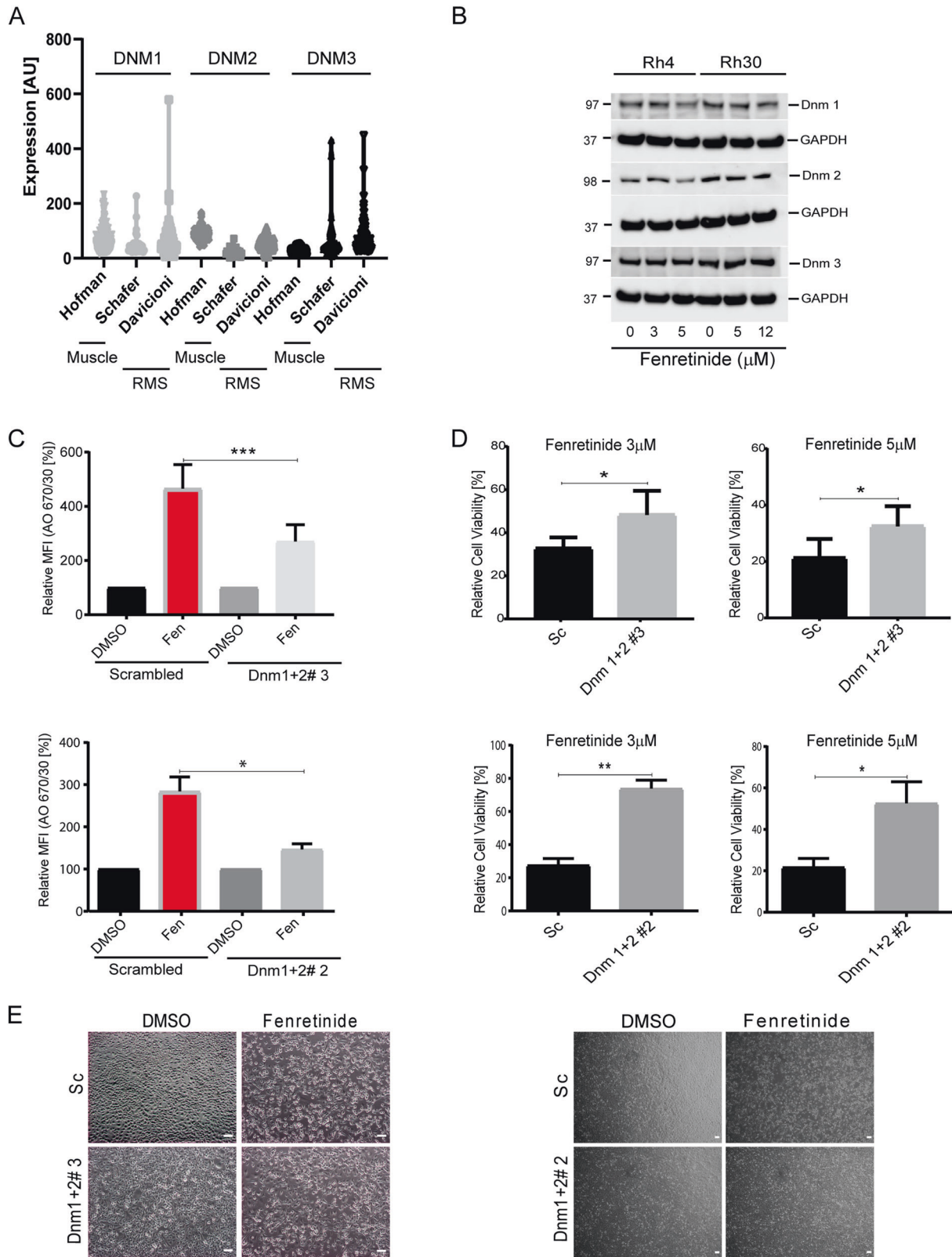
To validate the involvement of the dynamin GTPases in accumulation of endosomes, we first analyzed mRNA expression levels of the three dynamins in RMS tumor samples (datasets Schafer and Davicioni), in comparison with normal muscle tissue (Hofmann) using publically available datasets (<https://r2.amc.nl>) (Fig. 6a). This showed that all three dynamins are equally expressed in all samples. Next, we measured the effect of fenretinide on dynamin 1–3

mRNA and protein levels by qRT-PCR and western blot, respectively. While we observed a slight downregulation of both dynamin 1 and 2 protein, dynamin 1 mRNA levels were upregulated suggesting that dynamins are regulated at the posttranscriptional level in RMS cells. (Fig. 6b and Supplementary Fig. 7). Next, we knocked out dynamin 1 and 2 in both Rh4 and Rh30 cells via CRISPR/Cas9 engineering. The knockout in Rh4 cells was nearly complete for both dynamins, while efficiency was reduced in Rh30 cells for dynamin 1 (Supplementary Fig. 8A). Examining the uptake of AO after fenretinide treatment in dynamin knockout cells revealed a significant lower uptake compared with scrambled (sc) control cells (Fig. 6c and Supplementary Fig. 8B, C), demonstrating significant reduction of endocytic processes in knockout cells. Importantly, we also detected a significant rescue from cell death over different concentrations of fenretinide (Fig. 6d and Supplementary Fig. 8D), which was further confirmed by phase contrast images (Fig. 6e). Taken together, these findings indicate that the vesicle accumulation during fenretinide treatment is directly dependent on the dynamin GTPases. Furthermore, they suggest that the accumulation of the endosomes is causally and directly linked to cell death.

Discussion

One of the biggest therapeutic challenges in FP-RMS treatment is intrinsic or acquired resistance towards conventional therapies, which is the main cause for the high recurrence rates of this type of tumor. Since survival rates of patients with relapsed FP-RMS are still very poor [4], there is an urgent need to identify new agents that are effective against such resistant cells. Drugs that resensitize cells towards chemotherapy induced apoptosis as well as compounds that activate alternative, nonapoptotic cell death pathways represent potential opportunities in this context [33, 34]. Here, we characterized the cytotoxic effect of fenretinide on FP-RMS cells. Fenretinide was approved by the FDA for the treatment of childhood sarcomas in 2007. In our study, we used drug concentrations between 3 and 12 μ M to achieve macropinocytosis and cell death which is comparable with published data and in a well-tolerated range [35, 36].

Originally, fenretinide was detected as hit in a large compound library screen designed to identify drugs affecting PAX3-FOXO1 activity [25]. While fenretinide indeed affects PAX3-FOXO1 transcript levels, a more detailed characterization of the mechanism of action suggests that its cytotoxic effects in FP-RMS cells do not depend on reduction of PAX3-FOXO1 levels and therefore this might be a more downstream event following induction of cell death. Interestingly, fenretinide-induced cell death occurred



through a mechanism other than apoptosis, necroptosis, autophagy and ferroptosis, as neither commonly used inhibitors nor the genetic ablation of their key molecules

had a positive influence on survival of cells. In contrast, inhibition of ROS completely protected FP-RMS cells from fenretinide-mediated toxicity, as already described in other

◀ **Fig. 6 Inhibition of dynamin GTPases rescues from fenretinide-induced cell death.** **a** mRNA levels of dynamin 1, 2, and 3 in a muscle control set (Hofman) and two RMS tumor sets (Schafer and Davicioni). Data used were extracted from the R2 genomics analysis and visualization platform. **b** Western blot detection of dynamin 1–3 using whole-cell lysates from indicated Rh4 and Rh30 cells after treatment or not with increasing concentrations of fenretinide for 48 h. **c–e** Experiments using dynamin depleted cells generated by CRISPR/Cas9 and different sgRNAs. **c** Mean fluorescence index of the flow cytometry data of fenretinide (3 μ M) treated Rh4 and Rh30 dynamin depleted cells (upper and lower panel, respectively), stained with acridine orange (2.7 μ M) using two different bandpass filters 530/30 and 670/30 (See Supplementary Fig. 8B). **d** Cell viability of Rh4 and Rh30 dynamin depleted cells (upper and lower panel, respectively), treated with different concentrations of fenretinide. **e** Phase contrast images of Rh4 and Rh30 dynamin depleted cells left untreated or treated with fenretinide (3 and 4 μ M, respectively). Scale bar is 20 μ m.

cellular systems [37–40]. While it is not clear at this point how fenretinide induces ROS mechanistically, our study clearly demonstrates that ROS originating from the mitochondria plays an important and early role in fenretinide-mediated cell death in FP-RMS cells.

Multiple studies showed that lipid second messengers are targets of fenretinide, leading to ROS production. Ceramides, sphingolipid second messengers, can either be generated de novo or via hydrolysis of sphingomyelin and are implicated as signaling molecules during cell death [41]. Previously it was believed that fenretinide directly elevates ceramide, however newer studies using liquid chromatography-tandem mass spectrometry showed that it rather elevated its precursor dihydroceramide [42–44] via inhibition of dihydroceramide desaturase 1 [45]. Further, fenretinide was shown to activate 12-lipoxygenase through production of gangliosides [46] in neuroblastoma cells which also produced ROS [47, 48]. In addition, the DNA damage inducible transcription factor Gadd153 mRNA was destabilized in the presence of lipoxygenase inhibitors [49], which is upregulated in response to fenretinide treatment [50]. However, our data did not indicate an involvement of the sphingolipid pathway in fenretinide-induced cell death in ARMS cells, nor could the endoplasmic reticulum be linked to fenretinide-induced ROS and cell death.

Downstream of ROS, fenretinide induced the formation and accumulation of cytoplasmic vesicles. These vesicles are surrounded by a single membrane and therefore do not originate from the autophagy pathway which gives rise to double-membrane autophagosomes. Instead, the vesicles morphologically resembled endosomes, an interpretation which was further substantiated by fluid phase dye uptake studies showing strong enhancement of these processes by fenretinide. Furthermore, pharmacologic as well as genetic interference with dynamins blocked vesicle accumulation and rescued from fenretinide-induced cell death. The

dynamin GTPases are major mediators of endosome fission at the plasma membrane. They are involved in both clathrin-dependent and -independent endocytosis, but some evidence suggests that they also play a role in a specific macropinocytosis pathway involving circular dorsal ruffles (CDR) [51, 52]. Dynamin expression in tumor cells is comparable with the expression in muscle tissue. We found that inhibitors of clathrin and caveolin-mediated endocytosis like chlorpromazine, filipin, and genistein failed to block fenretinide-mediated cell death. Furthermore, ultrastructural analysis by EM showed that fenretinide-induced vesicles have a variable size with a diameter of up to 7 μ m, which is comparable with the described diameter of macropinosomes of 0.2–5 μ m [18]. Taken together, these data indicate that these vesicles most likely derive through an increased or impaired macropinocytosis.

Interestingly, blocking caspase activity by z-vad further enhanced the number of vesicles. Hence, while some cells might succumb by an apoptotic mechanism they will shift the mode of cell death when this route is blocked. This is in accordance with a delay in the onset of cell death by about 10 h in the presence of z-vad as seen in our time-lapse experiments. Also when compared with other cell death mechanisms, apoptosis is a relatively fast process [53, 54]. Accordingly, regulated, nonapoptotic modes of cell death such as necroptosis have only been detected after specific inhibitors of apoptosis became available [55, 56].

For induction of the vesicle associated type of cell death in FP-RMS cells, a special type of ROS stress seems to be relevant since induction of ROS-dependent cell death with other drugs including the proteasome inhibitors MLN2238 and MLN9708, the microtubule-destabilizing agent rigosertib or the selective inhibitor of nuclear export verdinexor were not blocked by dynamin inhibitors. The mechanisms behind these differences are currently unclear and will need further clarification in the future.

The role of ROS as important regulators of tyrosine kinase receptor signaling cascades [57–60], might be another possible explanation to the formation of CDRs after fenretinide treatment. Importantly, similar cellular phenotypes have been described in the context of different relatively vaguely described cell death mechanisms called paraptosis, oncosis, and methuosis [24, 26, 32]. In case of methuosis, vesicle accumulation has been associated with disturbance of endosomal maturation and/or recycling. Several different stimuli have been described that induce this phenotype, including different small molecules as well as activation of Ras, which stimulates macropinosome formation via overactivation of Rac1 and concomitant decline in Arf6, at the same time impeding their recycling (for review see Maltese et al. [17]). Ultimately, this manifests as vesicle accumulation as seen in different cells like glioblastoma, Ewing sarcoma and epithelial cells

[20, 26, 61]. Whether Ras mutant tumors compensate this effect and are less prone for methuosis is currently unclear. FP-RMS tumors are rarely associated with Ras mutations. Similar to methuosis, we observed an impaired recycling of endosomes with a maturation stop at the level of early/late endosome formation, as the vesicles acquire markers such as Rab5 and Rab7 but not the lysosomal marker LAMP-1. However, since pharmacological inhibition and knockout of Rac1 as well as Arf6 in FP-RMS cells neither affected fenretinide-mediated cell death nor dye uptake (data not shown), this pathway does not seem to play a major role. Hence, while the exact mechanisms leading to maturation stop of endosomes needs further characterization, it seems that different upstream pathways might be able to induce the same vacuolization phenotype associated with cell death. Importantly however, while in all the described cases vesicle accumulation and cell death correlate, a causal link of the two effects has not been established yet.

Overall, our results provide evidence that fenretinide-induced mitochondrial ROS interferes with regulation of dynamin-dependent macropinocytosis leading to vesicle accumulation in the cytoplasm of the cells. This is associated with a strong cytotoxic effect in FP-RMS cells. The fact that fenretinide engages a novel form of cell death which is not exploited by conventional chemotherapy agents defines it as a promising combinatorial partner for the treatment of FP-RMS patients. Agents for a potential combination treatment might be drugs that induce canonical apoptosis or necroptosis or even other forms of cell death like autophagy or ferroptosis. Since fenretinide is already in clinical use in children (Clinicaltrials.gov ID [NCT02163356](#)) and has only moderate side effects both in short- and long-term treatment regimens [35, 36] our findings might stimulate expansion of the clinical application of fenretinide to FP-RMS therapy in the future.

Material and methods

Cell culture

The aRMS cell lines RH4 and Rh30 (provided by Peter Houghton, Greehey Children's Cancer Research Institute, San Antonio, TX, USA) and the HEK293T (ATCC, LGC Promochem, Wesel, Germany) were maintained in Dulbecco's Modified Eagle Medium (DMEM, Sigma-Aldrich Buchs, Switzerland), with 100 U/mL penicillin/streptomycin (Invitrogen, ThermoFisher, Waltham, MA, USA), 2 mM L-glutamine (BioConcept, Allschwil, Switzerland) or Glutamax (Gibco, ThermoFisher, Waltham, MA, USA), and 10% fetal bovine serum (FBS) (Sigma-Aldrich Buchs, Switzerland), in 5% CO₂ at 37 °C. FP-RMS cell lines were

regularly tested for mycoplasma infection, authenticated by short tandem repeat analysis (STR profiling) in upon receipt in 2011/2014 and positively matched with reference data [62]. Frozen cell line stocks were used within 10–20 further passages.

Cell viability assay

Cells were seeded at a concentration of 3000 cells (Rh4) or 2000 cells (Rh30) in 384 well polystyrol microplates (Greiner Bio One, Kremsmünster, Austria) format in 20 µL medium.

For determination of dose-response curves with single compounds (see Table 1 in Supplementary Material and Methods), drugs were added to the cells using a HP D300 digital dispenser (Hewlett-Packard Development Company, L.P., Houston, TX, USA).

To assess metabolic activity 5 µL colorimetric WST-1 (Sigma-Aldrich, Buchs, Switzerland), diluted 1:1 with DMEM, was added. After 30 min of incubation at 37 °C in the dark, absorbance at 440 and 640 nm was measured with a Synergy™ HT multi-detection microplate reader (BioTek, Winooski, VT, USA). The difference of the two values was calculated (delta optical density; ΔOD) and values from pure medium were subtracted as background.

Small-molecule library screen

Cells were seeded at a concentration of 3000 cells (Rh4) or 2000 cells (Rh30) in 384 well polystyrol microplates (Greiner Bio One, Kremsmünster, Austria) format in 20 µL medium.

Drugs were diluted to a final concentration of 500 nM and manually added in duplicates to the cells (see Table 5 in the Supplementary Data and figures), 12 DMSO controls were included. After 48 h treatment, effects of drugs were determined by the cell viability assay.

Flow cytometry

For all flow cytometry experiments, 300'000 cells (Rh4) or 200'000 cells (Rh30) were seeded in Corning Costar six-well plates (Sigma-Aldrich, Buchs, Switzerland). After treatments, cells were detached from the plates using Trypsin, washed once with PBS and resuspended in 0.5 ml indicated buffer. Data were acquired with the LSRII Fortessa (BD Biosciences, San Jose, CA, USA) flow cytometer or the BD FACS Canto system (BD Biosciences, San Jose, CA, USA).

The data were analyzed with FlowJo Software, Version 9.9.6 (Tree Star Inc., Ashland, Orlando, USA). The used fluorescent stains can be found in Table 2 in Supplementary Material and Methods.

Pan-ROS measurement

Cells were seeded and treated with compounds according to Table 1 in Supplementary Material and Methods for 20–48 h. At the same time, CellRox Deep red (ThermoFisher, Waltham, MA, USA) solution (4 μ M) was added to the media. Cells were collected, washed in PBS (Sigma-Aldrich, Buchs, Switzerland) and resuspended in FluoroBrite DMEM live cell fluorescence imaging medium (ThermoFisher, Waltham, MA, USA). CellRox (ThermoFisher, Waltham, MA, USA) signal (50,000 events per sample) was acquired with excitation laser 640 nm and emission filter 670/14.

Mitochondrial ROS measurement

Cells were seeded and treated with the desired compounds according to Table 1 in Supplementary Material and Methods for 20–48 h. Cells were collected, washed in PBS and resuspended in MitoSox (ThermoFisher, Waltham, MA, USA) solution (10 μ M MitoSox in PBS) for 30 min at 37 °C in the dark. MitoSox signal (50,000 events per sample) was acquired with excitation laser 561 nm, and emission filter 570 LP, 525/50.

AO and LY uptake

Cells were seeded and treated with compounds according to Table 1 in Supplementary Material and Methods for 48 h. AO (2.7 μ M, Sigma-Aldrich, Buchs, Switzerland) and LY (820 μ M, ThermoFisher, Waltham, MA, USA) in FluoroBrite DMEM live cell fluorescence imaging medium (ThermoFisher, Waltham, MA, USA) was added to the cells 4 h prior to their preparation for flow cytometry after removal of the culture medium. Cells were collected, washed, and resuspended in PBS. Signals (50,000 events per sample) were acquired with excitation laser 488 nm and 561, emission filter 505LP, 530/30 and 635LP, 670/30 for AO and with excitation laser 405 nm, emission filter 505LP, 525/50 for LY.

Epifluorescence microscopy

All images were taken with a Zeiss Axio Observer microscope (Zeiss, Oberkochen, Germany) equipped with a Hamamatsu Orca Flash 4.0 V2, sCMOS cooled fluorescence camera (Hamamatsu, Hamamatsu City, Japan) and an objective with $\times 20$ magnification. The violet and green fluorescent filters were used for the imaging of DAPI, LY, Rab5/7, and Lamp-1 stained structures, respectively. Fluorophores are listed in Table 2 in Supplementary Material and Methods.

For data processing, images were exported as TIFF files and the mean integrated density was quantified with the image processing program Fiji [63]. The integrated density value of an image was divided by the number of cells (counted on phase contrast). A minimum of four pictures were taken for each treatment.

Rab5, Rab7, and Lamp-1 immunofluorescence staining

A total of 50,000 cells were seeded in four-well Falcon™ chambered cell culture slides (Thermo Scientific, ThermoFisher, Waltham, MA, USA) and treated with 3 μ M fenretinide for 48 h. After washing, cells were fixed with 4% paraformaldehyde (PFA) (Carl Roth, Karlsruhe, Germany), washed and quenched with 0.1 M glycine (Sigma-Aldrich, Buchs, Switzerland) in PBS. After fixing, cells were permeabilized with 0.1% triton X-100 (Sigma-Aldrich, Buchs, Switzerland) in PBS and then blocked with 4% horse serum (Sigma-Aldrich, Buchs, Switzerland) in 0.1% triton X-100/PBS before they were incubated with the respective primary antibody in 0.1% triton X-100 in PBS and 4% horse serum at 4 °C overnight in a humid chamber. Primary antibodies used for immunofluorescence localization of rabbit anti-Rab5 (Cat #2143) and rabbit anti-Rab7 (Cat #9367) were obtained from Cell Signaling Technology (Danvers, MA, USA) and mouse anti-LAMP-1 was obtained from the Developmental Studies Hybridoma Bank (University of Iowa, Ames, IA, USA), respectively. After three washing steps, cells were incubated with donkey anti-rabbit IgG-Alexa 488 (Rab5/7) or chicken anti-mouse IgG-Alexa 488 (Lamp-1) 2° Antibody (1:200) (both from ThermoFisher, Waltham, MA, USA) in PBS with 4% horse serum for 1 h at RT. After washing, the chamber walls were removed and cells were mounted using Vectashield mounting medium with 4',6-Diamidin-2-phenylindol (Vector Laboratories, Burlingame, CA, USA).

Live cell time-lapse microscopy

A total of 80,000 cells were seeded in 400 μ l of an eight-well 15u-Ibidi chambered cell culture slide (Ibidi GmbH, Planegg, Germany) and treated with or without 3 μ M fenretinide and different stains in FluoroBrite DMEM with 10% FBS and 1% Pen/Strep and L-glutamine. CellRox (4 μ M) was used for pan-ROS detection, PI (1 μ g/ml) (Sigma-Aldrich, Buchs, Switzerland) was used for detection of dead cells. For time-lapse image acquisition, the slides were kept in a thermally stabilized and CO₂ controlled chamber incubator (5% CO₂ at 37 °C) (Ibidi GmbH, Planegg, Germany) and images were automatically taken every 20 min over a 60 h period.

LY fluorescence microscopy

A total of 50,000 cells were seeded per well of a four-well Falcon™ chamber slide and treated with 3 μM or 4 μM (for Rh4 and Rh30, respectively) fenretinide for 48 h and subsequently stained with LY (820 μM) in FluoroBrite DMEM for 4 h at 37 °C and 5% CO₂. Afterwards, cells were washed with PBS and fixed with 4% PFA for 15 min at room temperature. After three PBS washes, the chamber was removed and the cells were mounted in Vectashield mounting medium with 4', 6-diamidin-2-phenylindol.

Electron microscopy

A total of 300,000 (Rh4) or 200,000 (Rh30) cells were seeded per well of a Corning Costar six-well plate (Sigma-Aldrich, Buchs, Switzerland) and treated with 3 or 5 μM fenretinide in combination with either 100 μM z-vad, 30 μM dynasore, 25 μM necrostatin, or 6.5 nM volasertib for 48 h at 37 °C, 5% CO₂. Treated and untreated control cells were then fixed with 2.5% glutaraldehyde (EMS Electron Microscopy Sciences, Hatfield, PA, USA) in 0.1 M cacodylate buffer (pH 7.35) (Merck AG, Zug, Switzerland) for at least an hour. Adherent cells were scraped off the culture dish using a cell scraper, combined with floating cells, pelleted by centrifugation and sequentially treated with 1% OsO₄ in 0.1 M cacodylate buffer for 1 h at 0 °C and 2% uranyl acetate (Merck AG, Zug, Switzerland) in H₂O overnight at 4 °C. The final pellet was immobilized with 2% Difco Noble Agar (BD Biosciences, Allschwil, Switzerland) in H₂O, subsequently dehydrated in an ethanol absolute series (VWR International GmbH, Dietikon, Switzerland) and embedded in Epon/Araldite (Sigma-Aldrich, Buchs, Switzerland). Ultrathin (50 nm) sections were contrasted with uranyl acetate and examined with a CM100 transmission electron microscope (Thermo Fisher Scientific, Eindhoven, The Netherlands) at an acceleration voltage of 80 kV using an Orius 1000 digital camera (Gatan, Munich, Germany), or a Talos 120 transmission electron microscope at an acceleration voltage of 120 KV using a Ceta digital camera and the MAPS software package (Thermo Fisher Scientific, Eindhoven, The Netherlands).

Immunoblotting

Whole-cell extracts were prepared from cells lysed with RIPA buffer (50 mM Tris-Cl (pH 7.5), 150 mM NaCl, 1% NP-40, 0.5% Na-deoxycholate, 1 mM EGTA, 0.1% SDS, 50 mM NaF, 10 mM sodium β -glycerolphosphate, 5 mM sodium pyrophosphate, 1 mM sodium orthovanadate), and supplemented with Complete Mini Protease Inhibitor cocktail (all from Sigma-Aldrich, Buchs, Switzerland). Proteins were separated using NuPAGE™ Novex™ 4-12%

Bis-Tris gels (ThermoFisher, Waltham, MA, USA) and transferred to nitrocellulose membranes (GE Healthcare Life Sciences). Membranes were blocked with 5% milk powder in TBS/0.05% tween and subsequently incubated with respective primary antibodies overnight at 4 °C. After three times washing in TBS-0.05% tween, membranes were incubated with horseradish peroxidase-linked secondary antibody for 1 h at RT. After three additional washing steps with TBS/0.05% tween, proteins were detected by chemiluminescence using either the Pierce™ ECL western blotting substrate or Supersignal western blotting reagent (both ThermoFisher, Waltham, MA, USA) and a ChemiDoc MP (BioRad Laboratories AG, Cressier, Switzerland) or Fuji-film LAS-3000 (Biocompare, San Francisco, USA) imager. The images were analyzed with the software Image Lab Version 6.0. (BioRad Laboratories AG, Cressier, Switzerland). All used antibodies are listed in Table 3 in Supplementary Material and Methods.

qRT-PCR

Total RNA was extracted from cells using the Qiagen RNeasy Kit (Qiagen, Hombrechtikon, Switzerland) and reverse-transcribed using random primers and Omniscript reverse transcriptase (Qiagen). qRT-PCR was performed using assay-on-demands (Life Technologies) for dynamin 1, 2, and 3 (Hs01074773_mH, Hs00974698_m1, and Hs00399015_m1) and TaqMan gene expression master mix (all Life Technologies). Cycle threshold (CT) values were normalized to GAPDH, relative expression levels were calculated using the $\Delta\Delta\text{CT}$ method. For statistical analysis *t*-test was performed using ΔCT values.

CRISPR/Cas9-mediated knockout

Multicolored lentiCRISPR plasmids with EGFP (Addgene Cat #75159), TagBFP (Addgene Cat #75160), or mCherry (Addgene Cat #75161) fluorescent markers were kindly provided by Scott McComb. The sgRNA sequences were designed on <http://crispr.mit.edu> (accessed 9.2.2017) and ordered as complementary oligos from Microsynth AG (Balgach, Switzerland) (for sgRNA sequences see Table 4 Supplementary Material and Methods). In total, 100 μM complementary oligos were annealed in Tango Buffer (ThermoFisher, Waltham, MA, USA) by heating for 5 min to 95 °C, followed by a slow cool down over 1 h to RT. Vectors, annealed sgRNA oligos, (ThermoFisher, Waltham, MA, USA), Esp3I (BsmBI) (ThermoFisher, Waltham, MA, USA), and T4 ligase (ThermoFisher, Waltham, MA, USA) were combined in T4 Ligase buffer and the following reaction was run on a T3000 thermocycler (Biometra, Biocompare, San Francisco, USA): ten cycles of 37 °C for 5 min and 16 °C for 10 min for restriction and

ligation, respectively. Four microliters of the ligation reaction was then used to transform Stellar™ competent bacteria (Clontech, Takara, Saint-Germain-en-Laye, France) by heat shock at 42 °C for 45 s (Clontech, Takara, Saint-Germain-en-Laye, France). Colony PCR using RedTaq PCR mixture (Sigma-Aldrich, Buchs, Switzerland) and sgRNA specific primers was performed to identify positive clones. For the production of lentiviral particles, 293T cells were transfected with the Lenti-CRISPR plasmid together with pVSV.G (Addgene Cat#8454) and pPAX (Addgene Cat#12260) plasmids in a ratio of 2.6:1:1 using either polyethylenimine (Polysciences, Warrington Township, PA, USA) or calcium phosphate (Sigma-Aldrich-Aldrich, Buchs, Switzerland). Medium was changed after 4 h, and virus was harvested 48 h later. Viral supernatants were concentrated using an Amicon Ultra tube Ultracel 100k (Millipore, Merck, Schaffhausen, Switzerland). For transduction of target cells, viral particles and 16 µg/ml hexadimethrine bromide (Sigma-Aldrich, Buchs, Switzerland) were added to culture medium and left overnight on the cells. After 72 h, transduction efficiency was evaluated by flow cytometry, and positive cells were isolated by FACS sorting with a BD Aria III 4L (BD Biosciences, San Jose, CA, USA). Several different sgRNAs per target gene were evaluated individually for their knockout efficiency and the two most efficient ones were selected for further experiments.

ShRNA-mediated knockdown

Custom lentiviral shRNA constructs containing a U6-tet promoter driven shRNA, either sc or directed against PAX3/FOXO1 (target sequence: GGCCTCTCACCTCAG AATTCA), as well as a PGK promoter driven GFP and puromycin expression cassette were purchased from Cellecta (Cellecta Inc. Mountain View, CA, USA). For constitutive expression of PAX3-FOXO1, the cDNA was cloned into the multiple cloning site (NheI) following the EF1 promoter in the lentiviral plasmid pRR-CMV-Bleo-EF1-MCS (Cellecta) also carrying a bleomycin resistance under a CMV promoter. Generation of lentiviral particles in HEK293T cells and transduction of the target cells was performed as described above for the CRISPR/Cas9 knockouts.

Statistical analysis

The software GraphPad Prism (La Jolla, CA, USA) was used for all statistical analysis (parametric paired *t*-test). The data were considered significant when $p \leq 0.05$. A minimum of three biological replicates were used.

Acknowledgements We thank Silvia Jenni, Gloria Pedot, and Luca Pontiggia (University Children's Hospital Zurich) for assistance with the cell sorting. This work was supported by the Krebsliga Zurich.

Compliance with ethical standards

Conflict of interest The authors declare that they have no conflict of interest.

Publisher's note Springer Nature remains neutral with regard to jurisdictional claims in published maps and institutional affiliations.

References

- Brien D, Jacob AG, Qualman SJ, Chandler DS. Advances in pediatric rhabdomyosarcoma characterization and disease model development. *Histol Histopathol.* 2012;27:13–22.
- Williamson D, Missiaglia E, de Reynies A, Pierron G, Thuille B, Palenzuela G, et al. Fusion gene-negative alveolar rhabdomyosarcoma is clinically and molecularly indistinguishable from embryonal rhabdomyosarcoma. *J Clin Oncol.* 2010;28:2151–8.
- Barr FG. Gene fusions involving PAX and FOX family members in alveolar rhabdomyosarcoma. *Oncogene.* 2001;20:5736–46.
- Dantonello TM, Int-Veen C, Schuck A, Seitz G, Leuschner I, Nathrath M, et al. Survival following disease recurrence of primary localized alveolar rhabdomyosarcoma. *Pediatr Blood Cancer.* 2013;60:1267–73.
- Kaufmann SH, Earnshaw WC. Induction of apoptosis by cancer chemotherapy. *Exp Cell Res.* 2000;256:42–9.
- Mesner PW Jr, Budihardjo II, Kaufmann SH. Chemotherapy-induced apoptosis. *Adv Pharmacol.* 1997;41:461–99.
- Fuchs J, Urla C, Sparber-Sauer M, Schuck A, Leuschner I, Klingebiel T, et al. Treatment and outcome of patients with localized intrathoracic and chest wall rhabdomyosarcoma: a report of the Cooperative Weichteilsarkom Studiengruppe (CWS). *J Cancer Res Clin Oncol.* 2018;144:925–34.
- Hanahan D, Weinberg RA. Hallmarks of cancer: the next generation. *Cell* 2011;144:646–74.
- Galluzzi L, Vitale I, Abrams JM, Alnemri ES, Baehrecke EH, Blagosklonny MV, et al. Molecular definitions of cell death subroutines: recommendations of the Nomenclature Committee on Cell Death 2012. *Cell Death Differ.* 2012;19:107–20.
- Vanden Berghe T, Kaiser WJ, Bertrand MJM, Vandenamee P. Molecular crosstalk between apoptosis, necroptosis, and survival signaling. *Mol Cell Oncol.* 2015;2:e975093.
- McComb S, Aguade-Gorgorio J, Harder L, Marovca B, Cario G, Eckert C, et al. Activation of concurrent apoptosis and necroptosis by SMAC mimetics for the treatment of refractory and relapsed ALL. *Sci Transl Med.* 2016;8:339ra70.
- Lin CY, Chang TW, Hsieh WH, Hung MC, Lin IH, Lai SC, et al. Simultaneous induction of apoptosis and necroptosis by Tanshinone IIA in human hepatocellular carcinoma HepG2 cells. *Cell Death Discov.* 2016;2:16065.
- Jing L, Song F, Liu Z, Li J, Wu B, Fu Z, et al. MLKL-PITPα signaling-mediated necroptosis contributes to cisplatin-triggered cell death in lung cancer A549 cells. *Cancer Lett.* 2018;414:136–46.
- Dixon Scott J, Lemberg Kathryn M, Lamprecht Michael R, Skouta R, Zaitsev Eleina M, Gleason Caroline E, et al. Ferroptosis: an iron-dependent form of nonapoptotic cell death. *Cell.* 2012;149:1060–72.
- Tsoi J, Robert L, Paraiso K, Galvan C, Sheu KM, Lay J, et al. Multi-stage differentiation defines melanoma subtypes with

- differential vulnerability to drug-induced iron-dependent oxidative stress. *Cancer Cell*. 2018;33:890–904.e5.
16. Hangauer MJ, Viswanathan VS, Ryan MJ, Bole D, Eaton JK, Matov A, et al. Drug-tolerant persister cancer cells are vulnerable to GPX4 inhibition. *Nature*. 2017;551:247–50.
 17. Maltese WA, Overmeyer JH. Methuosis: nonapoptotic cell death associated with vacuolization of macropinosome and endosome compartments. *Am J Pathol*. 2014;184:1630–42.
 18. Ahlstedt J, Fornvik K, Zolfaghari S, Kwak D, Hammarstrom LGJ, Ernfors P, et al. Evaluating vacuolin-1 in rats carrying glioblastoma models RG2 and NS1. *Oncotarget*. 2018;9:8391–9.
 19. Li Z, Mbah NE, Maltese WA. Vacuole-inducing compounds that disrupt endolysosomal trafficking stimulate production of exosomes by glioblastoma cells. *Mol Cell Biochem*. 2018;439:1–9.
 20. Manara MC, Terracciano M, Mancarella C, Sciandra M, Guerzoni C, Pasello M, et al. CD99 triggering induces methuosis of Ewing sarcoma cells through IGF-1R/RAS/Rac1 signaling. *Oncotarget*. 2016;7:79925–42.
 21. Sun L, Li B, Su X, Chen G, Li Y, Yu L, et al. An ursolic acid derived small molecule triggers cancer cell death through hyperstimulation of macropinocytosis. *J Med Chem*. 2017;60:6638–48.
 22. Aki T, Nara A, Uemura K. Cytoplasmic vacuolization during exposure to drugs and other substances. *Cell Biol Toxicol*. 2012;28:125–31.
 23. Weerasinghe P, Buja LM. Oncosis: an important non-apoptotic mode of cell death. *Exp Mol Pathol*. 2012;93:302–8.
 24. Sperandio S, de Belle I, Bredesen DE. An alternative, non-apoptotic form of programmed cell death. *Proc Natl Acad Sci USA*. 2000;97:14376–81.
 25. Herrero Martin D, Boro A, Schafer BW. Cell-based small-molecule compound screen identifies fenretinide as potential therapeutic for translocation-positive rhabdomyosarcoma. *PLoS ONE*. 2013;8:e55072.
 26. Overmeyer JH, Kaul A, Johnson EE, Maltese WA. Active ras triggers death in glioblastoma cells through hyperstimulation of macropinocytosis. *Mol Cancer Res*. 2008;6:965–77.
 27. Bernasconi M, Remppis A, Fredericks WJ, Rauscher FJ 3rd, Schafer BW. Induction of apoptosis in rhabdomyosarcoma cells through down-regulation of PAX proteins. *Proc Natl Acad Sci USA*. 1996;93:13164–9.
 28. Ommer J, Selve J, Wachtel M, O'Brien E, Laubscher D, Roemmele M, et al. Aurora A kinase inhibition destabilizes PAX3-FOXO1 and MYCN and synergizes with Navitoclax to induce Rhabdomyosarcoma cell death. *Cancer Res*. 2019;80:832–42.
 29. Dixon SJ, Lemberg KM, Lamprecht MR, Skouta R, Zaitsev EM, Gleason CE, et al. Ferroptosis: an iron-dependent form of non-apoptotic cell death. *Cell*. 2012;149:1060–72.
 30. Dixon SJ, Patel DN, Welsch M, Skouta R, Lee ED, Hayano M, et al. Pharmacological inhibition of cystine-glutamate exchange induces endoplasmic reticulum stress and ferroptosis. *Elife*. 2014;3:e02523.
 31. Zheng DW, Xue YQ, Li Y, Di JM, Qiu JG, Zhang WJ, et al. Volasertib suppresses the growth of human hepatocellular carcinoma in vitro and in vivo. *Am J Cancer Res*. 2016;6:2476–88.
 32. Shubin AV, Demidyuk IV, Komissarov AA, Rafieva LM, Kostrov SV. Cytoplasmic vacuolization in cell death and survival. *Oncotarget*. 2016;7:55863–89.
 33. Fulda S. Targeting apoptosis resistance in rhabdomyosarcoma. *Curr Cancer Drug Targets*. 2008;8:536–44.
 34. Fulda S. Therapeutic opportunities based on caspase modulation. *Semin Cell Dev Biol*. 2017;82:150–7.
 35. Cooper JP, Reynolds CP, Cho H, Kang MH. Clinical development of fenretinide as an antineoplastic drug: pharmacology perspectives. *Exp Biol Med*. 2017;242:1178–84.
 36. Mohrbacher AM, Yang AS, Groshen S, Kummar S, Gutierrez ME, Kang MH, et al. Phase I study of fenretinide delivered intravenously in patients with relapsed or refractory hematologic malignancies: a California cancer consortium trial. *Clin Cancer Res*. 2017;23:4550–5.
 37. Chen NE, Maldonado NV, Khankaldyyan V, Shimada H, Song MM, Maurer BJ, et al. Reactive oxygen species mediates the synergistic activity of fenretinide combined with the microtubule inhibitor ABT-751 against multidrug-resistant recurrent neuroblastoma xenografts. *Mol Cancer Ther*. 2016;15:2653–64.
 38. Asumendi A, Morales MC, Alvarez A, Arechaga J, Perez-Yarza G. Implication of mitochondria-derived ROS and cardiolipin peroxidation in N-(4-hydroxyphenyl)retinamide-induced apoptosis. *Br J Cancer*. 2002;86:1951–6.
 39. Cupeper R, Leen R, Tytgat GAM, Caron HN, van Kuilenburg ABP. Fenretinide induces mitochondrial ROS and inhibits the mitochondrial respiratory chain in neuroblastoma. *Cell Mol Life Sci*. 2010;67:807–16.
 40. Makena MR, Koneru B, Nguyen TH, Kang MH, Reynolds CP. Reactive oxygen species-mediated synergism of fenretinide and romidepsin in preclinical models of T-cell lymphoid malignancies. *Mol Cancer Ther*. 2017;16:649–61.
 41. Lee J, Yeganeh B, Ermini L, Post M. Sphingolipids as cell fate regulators in lung development and disease. *Apoptosis*. 2015;20:740–57.
 42. Zheng W, Kollmeyer J, Symolon H, Momin A, Munter E, Wang E, et al. Ceramides and other bioactive sphingolipid backbones in health and disease: lipidomic analysis, metabolism and roles in membrane structure, dynamics, signaling and autophagy. *Biochim Biophys Acta*. 2006;1758:1864–84.
 43. Hail N Jr, Chen P, Kepa JJ, Bushman LR, Shearn C. Dihydroorotate dehydrogenase is required for N-(4-hydroxyphenyl)retinamide-induced reactive oxygen species production and apoptosis. *Free Radic Biol Med*. 2010;49:109–16.
 44. Hail N Jr, Kim HJ, Lotan R. Mechanisms of fenretinide-induced apoptosis. *Apoptosis*. 2006;11:1677–94.
 45. Rahmaniyan M, Curley RW Jr, Obeid LM, Hannun YA, Kravaka JM. Identification of dihydroceramide desaturase as a direct in vitro target for fenretinide. *J Biol Chem*. 2011;286:24754–64.
 46. Lovat PE, et al. The role of gangliosides in fenretinide-induced apoptosis of neuroblastoma. *Cancer Lett*. 2005;228:105–10.
 47. Lovat PE, Di Sano F, Corazzari M, Fazi B, Donnorso RP, Pearson AD, et al. Gangliosides link the acidic sphingomyelinase-mediated induction of ceramide to 12-lipoxygenase-dependent apoptosis of neuroblastoma in response to fenretinide. *J Natl Cancer Inst*. 2004;96:1288–99.
 48. Lovat PE, Ranalli M, Corazzari M, Raffaghello L, Pearson AD, Ponzoni M, et al. Mechanisms of free-radical induction in relation to fenretinide-induced apoptosis of neuroblastoma. *J Cell Biochem*. 2003;89:698–708.
 49. Lai WL, Wong NS. ROS mediates 4HPR-induced posttranscriptional expression of the Gadd153 gene. *Free Radic Biol Med*. 2005;38:1585–93.
 50. Lovat PE, Oliverio S, Corazzari M, Ranalli M, Pearson AD, Melino G, et al. Induction of GADD153 and Bak: novel molecular targets of fenretinide-induced apoptosis of neuroblastoma. *Cancer Lett*. 2003;197:157–63.
 51. Orth JD, Krueger EW, Weller SG, McNiven MA. A novel endocytic mechanism of epidermal growth factor receptor sequestration and internalization. *Cancer Res*. 2006;66:3603–10.
 52. Orth JD, McNiven MA. Get off my back! Rapid receptor internalization through circular dorsal ruffles. *Cancer Res*. 2006;66:11094–6.
 53. Coultas L, Strasser A. The molecular control of DNA damage-induced cell death. *Apoptosis*. 2000;5:491–507.
 54. Galluzzi L, Vitale I, Aaronson SA, Abrams JM, Adam D, Agostinis P, et al. Molecular mechanisms of cell death:

- recommendations of the Nomenclature Committee on Cell Death 2018. *Cell Death Differ.* 2018;25:486–541.
55. Hirsch T, Marchetti P, Susin SA, Dallaporta B, Zamzami N, Marzo I, et al. The apoptosis-necrosis paradox. Apoptogenic proteases activated after mitochondrial permeability transition determine the mode of cell death. *Oncogene.* 1997;15:1573–81.
 56. Degterev A, Huang Z, Boyce M, Li Y, Jagtap P, Mizushima N, et al. Chemical inhibitor of nonapoptotic cell death with therapeutic potential for ischemic brain injury. *Nat Chem Biol.* 2005;1:112–9.
 57. Aslan M, Ozben T. Oxidants in receptor tyrosine kinase signal transduction pathways. *Antioxid Redox Signal.* 2003;5:781–8.
 58. Ha SJ, Lee J, Park J, Kim YH, Lee NH, Kim YE, et al. Syringic acid prevents skin carcinogenesis via regulation of NoX and EGFR signaling. *Biochem Pharmacol.* 2018;154:435–45.
 59. Paulsen CE, Truong TH, Garcia FJ, Homann A, Gupta V, Leonard SE, et al. Peroxide-dependent sulfenylation of the EGFR catalytic site enhances kinase activity. *Nat Chem Biol.* 2011;8:57.
 60. Irani K, Xia Y, Zweier JL, Sollott SJ, Der CJ, Fearon ER, et al. Mitogenic signaling mediated by oxidants in Ras-transformed fibroblasts. *Science.* 1997;275:1649–52.
 61. Dendo K, Yugawa T, Nakahara T, Ohno SI, Goshima N, Arakawa H, et al. Induction of non-apoptotic programmed cell death by oncogenic RAS in human epithelial cells and its suppression by MYC overexpression. *Carcinogenesis.* 2018;39:202–13.
 62. Hinson AR, Jones R, Crose LE, Belyea BC, Barr FG, Linardic CM. Human rhabdomyosarcoma cell lines for rhabdomyosarcoma research: utility and pitfalls. *Front Oncol.* 2013;3:183.
 63. Schindelin J, Arganda-Carreras I, Frise E, Kaynig V, Longair M, Pietzsch T, et al. Fiji: an open-source platform for biological-image analysis. *Nat Methods.* 2012;9:676–82.